



Selective femtosecond laser ablation via two-photon fluorescence imaging through a multimode fiber

EIRINI KAKKAVA,^{1,*} MARILISA ROMITO,¹ DONALD B. CONKEY,¹ DAMIEN LOTERIE,² KONSTANTINA M. STANKOVIC,³ CHRISTOPHE MOSER,² AND DEMETRI PSALTIS¹

¹Optics Laboratory, School of Engineering, École Polytechnique Fédérale De Lausanne, Lausanne, Switzerland

²Laboratory of Applied Photonic Devices, School of Engineering, École Polytechnique Fédérale De Lausanne, Lausanne, Switzerland

³Department of Otolaryngology and Eaton Peabody Laboratories, Massachusetts Eye and Ear and Harvard Medical School, Boston, MA, USA

*eirini.kakkava@epfl.ch

Abstract: We demonstrate the ability of a multimode fiber probe to provide two-photon fluorescence (TPF) imaging feedback that guides the femtosecond laser ablation (FLA) in biological samples for highly selective modifications. We implement the system through the propagation of high power femtosecond pulses through a graded-index (GRIN) multimode fiber and we investigate the limitations posed by the high laser peak intensities required for laser ablation. We demonstrate that the GRIN fiber probe can deliver laser intensities up to 1.5×10^{13} W/cm², sufficient for the ablation of a wide range of materials, including biological samples. Wavefront shaping through an ultrathin probe of around 400 μ m in diameter is used for diffraction limited focusing and digital scanning of the focus spot. Selective FLA of cochlear hair cells is performed based on the TPF images obtained through the same multimode fiber probe.

© 2019 Optical Society of America under the terms of the [OSA Open Access Publishing Agreement](#)

1. Introduction

Optical fibers are important clinical tools because they allow access to confined places in a minimally invasive way. In the current clinical practice, optical fibers deliver and retrieve light from the area of interest; increasingly, fiber probes are also used as surgical tools [1]. Meanwhile, ultrashort pulses have revolutionized conventional microscopy using nonlinear optical phenomena to improve the resolution and quality of the obtained images, such as two-photon fluorescence (TPF) [2,3] and second-harmonic generation (SHG) [4,5]. Ultrashort pulse delivery through fiber probes has made these imaging modalities endoscopically configurable [6–9]. Apart from nonlinear microscopy, femtosecond laser ablation (FLA) has been also extensively used in medicine due to its high precision and minimal collateral damage [10–13]. However, the peak intensities needed to perform FLA can exceed the tolerance of common endoscopes. With at least two-orders of magnitude more peak intensity than what is needed for TPF imaging ($\sim 10^9$ W/cm²), FLA may induce nonlinearities or even fiber damage [14]. Hollow-core photonic crystal fibers (HC-PCFs) have been proposed to efficiently deliver high power femtosecond pulses for laser ablation [15–18]. The femtosecond pulses are guided in air or gas in the case of HC-PCF, thus nonlinear effects do not significantly affect the pulse delivery. Micro-Joule pulse energy delivery has been reported for the HC-PCFs which is sufficient to perform laser ablation. However, further increase in the input pulse energy is limited by the nonlinearities and damage that can arise in the optics and scanning mechanism at the distal end that are necessary for focusing the light

[17]. For combining imaging and ablation, the use of HC-PCFs can be also limited by the narrow bandwidth, which restricts the fluorescence collection to certain wavelengths.

Most commercially available tools use either single mode fibers (SMFs) combined with optical components to focus the light at the distal side and scanning mechanisms to steer the light around the region of interest or fiber bundles that result in pixelated images [1,17,19–22]. The addition of distal end optical and/or mechanical components significantly increases the size and complexity of the endoscope. To avoid this, wavefront shaping techniques (digital-phase conjugation (DPC), transmission matrix (TM), iterative optimization) have been proposed to focus and scan the laser beam digitally by encoding the wavefront at the proximal end of a multimode fiber (MMF) [20,23–29]. In this work, we use the TM technique to focus and scan the light through ultrathin GRIN fibers. We use two GRIN fibers of 200 μm and 400 μm diameter core size to test their performance in delivering a high peak intensity femtosecond focus spot for laser ablation applications in biological samples. Our results show that the 400 μm diameter GRIN fiber can provide a focus spot with peak intensities reaching up to $1.5 \times 10^{13} \text{ W/cm}^2$. The peak intensity delivered by our system is comparable to that of a HC-PCF [17,18], while maintaining the size of the final probe below 1mm by avoiding the need of distal components.

Multimodal endoscopes have been proposed [30,31] for acquiring images with several techniques integrated in the same probe. In this paper, we report for the first time FLA through multimode fibers combined with TPF imaging through the same multimode fiber. We test the performance of our dual-modality endoscopic tool in the organ for hearing (Organ of Corti) from an extracted mouse cochlea. The Organ of Corti includes mechanosensory cells, named hair cells, which are responsible for the detection and transduction of sounds. TPF images of the cochlear hair cells were acquired through our endoscope and used to define the area of interest that is then ablated through the same tool. By developing a technique with imaging modalities integrated with selective laser ablation capabilities, we provide a minimally invasive system for both cellular level investigation of distinct target areas and for cell manipulation.

2. Optical setup

For the implementation of the TM measurement setup (Fig. 1) we used a high pulse energy laser system (Satsuma, Amplitude Systèmes, $\lambda = 1030 \text{ nm}$, $E_{\text{pulse,max}} = 40 \mu\text{J}$) that provides tunable pulse duration. The repetition rate is set at 20 kHz. After the laser beam is expanded and collimated by combining two achromatic lenses (L1: $f = 50 \text{ mm}$, L2: $f = 150 \text{ mm}$) at the output of the laser, it is split into illumination and reference paths using a polarizing beam splitter (PBS, Fig. 1). In the illumination path, the laser beam is reflected by a spatial light modulator (SLM, Pluto-NIR2, Holoeye) and the SLM plane is imaged using a 4f system at the proximal facet of the optical fiber. The 4f system was optimized so that the SLM plane is demagnified approximately to fit the size of the fiber core. In the case of 200 μm core GRIN fiber the 4f system consists of the achromatic lens L3 ($f = 300 \text{ mm}$) and a 20x (0.4 NA, Newport) microscope objective (O1), while for the 400 μm core fiber the focal length of L3 was changed to 150 mm. The size of the laser beam at the SLM plane was 8mm to exploit most of the pixels available and to avoid damage of the device at the high pulse energy levels. Even at the maximum pulse energy used in the experiments ($E_p = 15 \mu\text{J}$) the peak intensity at the SLM plane was in the order of 60 MW/cm^2 , which is much lower than the damage threshold of the device ($\sim 0.25 \text{ TW/cm}^2$). A second 4f system is placed at the distal facet to image the output of the fiber on a CMOS (MV1-D1312IE-G2-12, PhotonFocus) detector array. For the second 4f system a 40x (0.65 NA, Newport) microscope objective (O2) was combined with an achromatic lens (L4) of 125mm focal length. We chose a higher NA microscope objective at the distal side of the fiber to collect the most of the high frequency components of the output field. The reference beam is also directed on the CMOS where it interferes with the fiber output resulting in a digital hologram. A delay line in the reference

path allows adjusting the path length to achieve coherence gating of the fiber output pulse. We use two 10 cm long GRIN fibers of 200 μm and 400 μm core size (by Fiberware) with a numerical aperture (NA) of 0.29, which support about 7800 and 31,200 spatial modes respectively, at the operating wavelength.

During the calibration process, plane waves at different angles are sequentially projected with the SLM and the corresponding hologram for the speckle pattern at the distal end of the fiber is recorded on the CMOS detector for each input angle. The amplitude and phase of the distal field are then holographically extracted for each angle constructing the TM of the system. After the TM is inverted, any desired output can be generated by calculating the proximal phase on the SLM as a combination of input angles. The number of input angles used for the two GRIN fibers, 200 μm and 400 μm core diameter, is chosen to be higher than the number of modes that the fiber supports to ensure that we maximally utilize the capability of the fiber. The TM is calculated using 12,000 and 46,000 input angles for each of the fibers respectively [32]. More details concerning the TM recording and processing have been previously reported [24,25,33]. The pulse energy used for measuring the TM ($E_p = 0.2 \mu\text{J}$) was below the level that nonlinearities arise along the GRIN fibers.

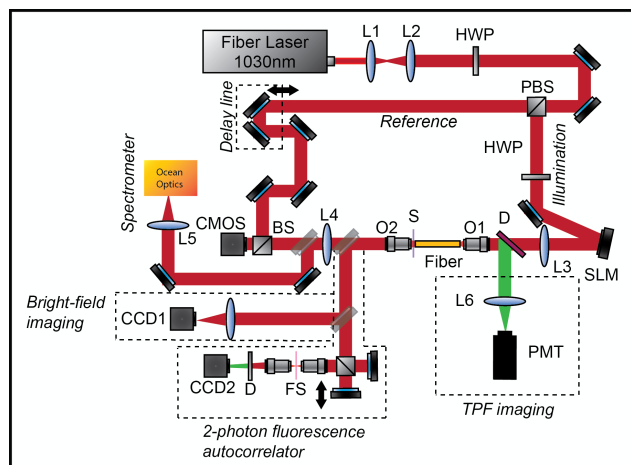


Fig. 1. Transmission matrix experimental setup for focusing and scanning the light through the optical fibers, combined with a TPF autocorrelator and a spectrometer for characterizing the temporal and spectral profile of the pulse and a TPF imaging part for the creation of the sample images. (S = sample, D = dichroic, HWP = half-wave plate, FS = fluorescent sample for TPF autocorrelator, O = microscope objective, L = lens, PBS = polarizing beam splitter, BS = beam splitter)

For the characterization of the performance of the GRIN fibers at high peak intensities needed for laser ablation of materials, we study the temporal and spectral profiles of the focused pulse at the distal side at different input pulse energies. The pulse duration of the laser focus is measured by a two-photon interferometric autocorrelator that is integrated into the system. Two microscope objectives of 40x magnification (0.65 NA, Newport) were used for focusing and collecting the light from the fluorescence sample (Rhodamine 6G in SU8) on CCD2 (Chameleon 3, Point Grey Research). The beam is redirected into the autocorrelator path by a flip mirror (Fig. 1). The spectral characteristics of the distal output are measured using a spectrometer (HR4000CG-UV-NIR, Ocean Optics) which is placed in the conjugate plane of the focus spot. For the TPF measurements, a dichroic mirror (D) and a photomultiplier (PMT, Hamamatsu, H11526-20-NN) are also integrated in the proximal side of the fiber so that the fluorescent signal emitted by the sample is collected back to form an image. The fluorescence signal was focused on the PMT by means of 100 mm lens. A bright field (BF) imaging block is also set in transmission from the sample to monitor the areas of

interest consisting of a lens of 300 mm focal length to form an image on the CCD1(Chameleon 3, Point Grey Research) as shown in Fig. 1.

3. Cochlear sample preparation

Four ten-week old mice (NMRI strain) are used in this study. All animal procedures are approved by Ecole Polytechnique Fédérale de Lausanne (EPFL). The mouse is sacrificed, intracardially perfused and the cochlea is removed. Under the operating microscope, the middle turn of the cochlear bone is carefully opened with forceps while leaving the inner soft structures intact. The cochlea is then fixed in cold 4% paraformaldehyde (PFA) in 0.1 M phosphate-buffered saline (PBS) for 30 min and rinsed with PBS three times for 5 minutes each. The remaining cochlear bone is gently removed and the pieces of Organ of Corti were microdissected. The Organ of Corti pieces are permeabilized in 0.3% Triton-X 100 for 15 minutes, rinsed with PBS, and stained with propidium iodide (PI, Thermofisher Scientific, 1:100 dilution of 1.5 mM stock solution) - a popular red-fluorescent ($\lambda_{em,max} = 617$ nm) nuclear stain. After 30 minutes, the stained samples are rinsed with PBS three times for 5 minutes each, mounted in ProLong Diamond media (from Life Sciences Technologies), sealed between two thin coverslips (145 μ m) and imaged using the setup schematized in Fig. 1. The prepared sample was extracted from the middle turn of the cochlea and its thickness is about 100 μ m.

4. High peak intensity delivery through GRIN fibers

We have previously reported on the delivery of ultrashort pulses via a multicore fiber (MCF) for laser ablation purposes [25]. We achieved a maximum peak intensity delivery of 4×10^{12} W/cm² with a MCF fiber of 10,000 cores (460 μ m core diameter) [25]. The segmented (grating-like) core shape of the MCFs results in the formation of a diffraction circle around the focus spot even after wavefront shaping, which reduces the light power in the focus to about 14% of the total power [25,34–36]. The percentage of laser power at the distal side that reaches the focus spot is defined as the focusing efficiency of the system. To improve peak power delivered in a focused ultrashort pulse through a fiber endoscope, we investigate the focusing efficiency of different kinds of fibers. Step index MMFs are excluded because of the high modal dispersion which enables probing of only few modes using coherent gating at the output. Therefore, two GRIN fibers with 200 μ m and 400 μ m core diameter are selected and tested. For each of the two fibers, we measure the dependence of the focusing efficiency on the input power for three different input pulse durations (Fig. 2). A high intensity focus spot is generated at the distal fiber end after measuring the TM of the system. The maximum value of the focusing efficiency was found to be ~28% for both probes, which is significantly higher than that achieved by the MCFs. In the case of an ideal Airy spot 84% of the total power should be concentrated in the central lobe. However, in our experiments, we probe only one polarization and a fraction of the total modes is not included in the measurement. By rotating a linear polarizer placed in front of the CMOS detector we observe that the output is elliptically polarized which implies that more than half of the modes should be probed in terms of polarization. Apart from the loss of a number of modes because of the polarization selectivity, the coherence gating of the fiber output also reduces the number of contributing modes on the formation of a focus spot at the fiber distal end. As a result, the focusing efficiency achieved is limited at about 28% which can be considered optimal if taking into account the losses explained above. The light is focused at 200 μ m from the distal fiber in a spot with 2.3 μ m full-width at half maximum (FWHM). The spot size is slightly larger than the theoretical value (Rayleigh criterion) which is calculated to be 2.17 μ m for the NA of the fiber (NA = 0.29) and the laser wavelength we use in the experiments. The deviation could be attributed to the fact that higher order modes are not probed by the system resulting in a lower effective NA [20,37–39].

For focusing the light through the GRIN fiber, the phase input on the SLM is calculated using the measured TM so that the ideal quadratic phase is created at the distal facet. When this phase profile is launched at the proximal side of the fiber, the light becomes distributed among the supported fiber modes and each one propagates through the system with a certain initial phase assigned by the wavefront-shaped input. The TM is a method applied to linear systems and its validity and performance deviate when nonlinear phenomena occur [25,40,41]. When the laser pulse energy exceeds a certain threshold then nonlinear phenomena such as self-phase modulation (SPM) and cross-phase modulation (XPM) can arise. The spectral measurements for the 200 μm core fiber showed spectral broadening of 9 nm confirming the presence of nonlinearities. However, no side bands were present in the spectrum, which would imply Four-Wave Mixing or Raman scattering nonlinear effects [14,42]. The maximum phase shift induced by these phenomena affects the relative phase among the modes along the propagation and as a result, the final phase profile at the distal facet is different from the optimized by the linear TM, which will reduce the final focusing efficiency [14]. Considering the dependence of the SPM and XPM phase shift on the fiber length [14], an increase of the fiber length would result in an increase of the nonlinear effect on the system's efficiency for focusing the light at the distal side. In our past work, we studied the dependence of the focusing efficiency of a MCF system for three different fiber lengths (10, 20 and 30 cm) and we observed a degradation for the longer segments [43]. Moreover, for practical applications, where the fiber probe inserted in a cannula would be a part of a hand-held device 10-20 cm length is sufficient to reach most of the areas of interest. Therefore, we selected the 10 cm long GRIN fiber for our experiments.

Based on the discussion above, at high energy input pulses, nonlinearities arise and affect the propagation of the input field along the fiber, resulting in scrambling of the optimized wavefront at the distal facet and compromising the focusing efficiency (Fig. 2) [14,25]. Because nonlinear phenomena are intensity dependent, the smaller the fiber core and the shorter the pulse duration is for a given input pulse energy, the more significant the nonlinear effects. We studied the performance of the two fiber probes as a function of pulse duration for three cases, 500 fs, 700fs and 1000fs pulses. The focusing efficiency of a 200 μm core diameter GRIN fiber diminishes rapidly after a certain threshold ($\sim 1 \mu\text{J}$) (Fig. 2(a)), while the 400 μm core fiber (Fig. 2(c)) shows a linear behavior for a wider range of input pulse energies [25]. As a result, increase in the input energy does not lead to a further increase in the final peak intensity in the focus for the thinner fiber (Fig. 2(b)). For calculating the peak intensity of the focus spot for the different input pulse energies, the pulse duration of the fiber output was measured using TPF-based autocorrelator. The spot size was measured on the CMOS for different input pulse energies (0.2, 1, 4.6 and 8.8 μJ) and no change was observed. For a 200 μm core fiber, nonlinearities cause temporal and spectral broadening when the power is increased above a certain level. For example, for 500 fs input pulse, the measured output pulse increases to about 700 fs when the input energy reaches 6 μJ , while the spectral width increases from 8 nm to 17 nm. The degradation of the focus spot efficiency because of the nonlinearities in the 200 μm core GRIN fiber lead to a saturation of the peak intensity that can be delivered through the system to a maximum value of $\sim 2.5\text{-}3 \times 10^{12} \text{ W/cm}^2$. The maximum delivered peak intensity by the 200 μm core GRIN fiber is comparable to the one achieved using the MCF of double the core size (460 μm) [25], which demonstrates that the ultrashort pulse delivery is more efficient for GRIN fibers. Further increase in the input power resulted in focusing inside the fiber itself creating fiber damage. For the 400 μm core fiber, no significant decrease in the focusing efficiency was observed for the range of input energies that we studied, including when the shortest pulse duration (500 fs) was tested. In addition, temporal and spectral measurements of the focus spot showed no change even at the highest input pulse energy. Consequently, the peak intensity delivered by this probe shows a linear increase throughout the range studied for the 700 fs and 1000 fs input pulses. In the case of 500 fs input pulse duration a saturation of the delivered peak intensity is observed above 6 μJ .

For the highest input power provided by the laser system used for the measurements, the maximum peak intensity measured was $1.5 \times 10^{13} \text{ W/cm}^2$ (Fig. 2(d)).

In addition, further increase of the maximum peak intensity delivered by both systems could be achieved by prechirping the pulse at the input. In this way, pulse broadening because of group velocity dispersion (GVD) could be compensated and nonlinearities would be less significant for the stretched pulse [7]. Nevertheless, the resulting peak intensities of both systems are promising for multiphoton imaging applications and open the path for processing materials with a wide range of ablation thresholds, from metals and polymers ($\sim 10^{10} \text{ W/cm}^2$), tissue ($\sim 10^{12} \text{ W/cm}^2$) and glass ($\sim 10^{13} \text{ W/cm}^2$).

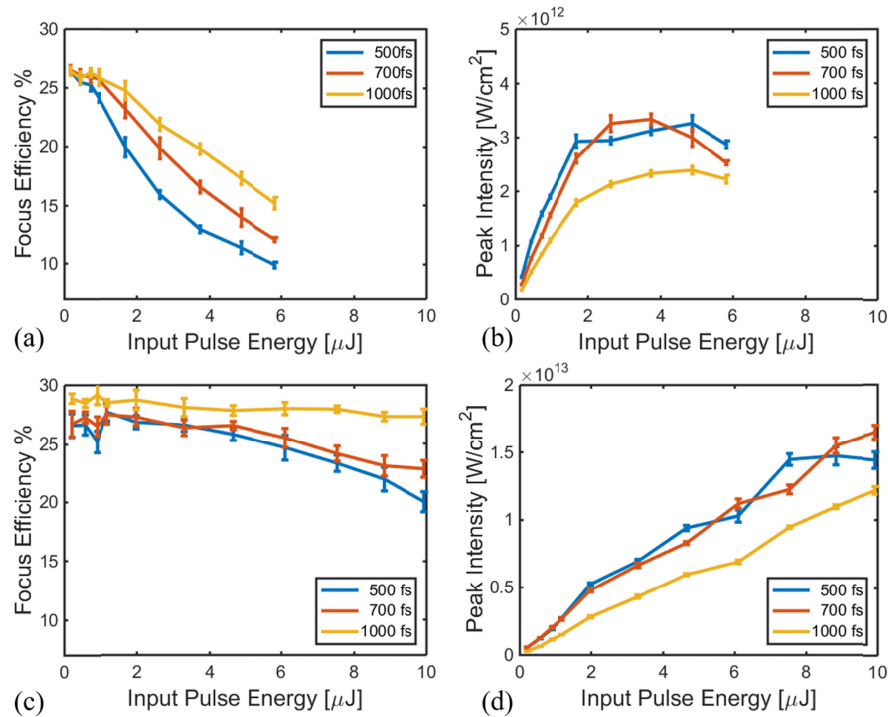


Fig. 2. Characterization of the 200 μm (a and b) and 400 μm (c and d) core diameter fibers. (a and c) Focusing efficiency for the 200 μm and the 400 μm core GRIN fiber respectively, and (b and d) the corresponding peak intensity delivered at the distal spot as a function of input pulse energy for each of the two systems respectively.

Both GRIN probes studied in this work show high performance for delivery of focused femtosecond pulses for laser ablation or imaging applications that is comparable to the one achieved using HC-PCFs. Specifically, Kagome HC-PCFs have shown unsurpassed ability to deliver ultrashort pulses, reaching peak intensities of $4 \times 10^{13} \text{ W/cm}^2$. Debord et al. [18] demonstrated glass processing using the fundamental mode of a Kagome HC-PCF with no distal components. However, the feature size in this case depends on the mode diameter, which is about 50 μm for a 19-cell Kagome HC-PCF design. For endoscopic application, these fibers have been used to build a microsurgery scalpel by Subramanian et al. [17] and the maximum peak intensity delivered is reported to be about $5 \times 10^{12} \text{ W/cm}^2$ in a focus spot of 2.5 μm size. The need of distal lenses for focusing the light emerging from the fiber comprises the maximum intensity that the endoscope can handle due to the nonlinearities raised when high-energy pulses propagate through the optical elements. Recently, the use of different lens material showed that the power throughput can be further increased for a HC-PCF endoscope [7,38,39]. However, the combination of distal lenses and a piezo-based scanning mechanism result in an increased size of the endoscope to 5mm if compared to the original fiber diameter

which is few hundreds microns. In our case, both GRIN fiber probes provide more than 2×10^{12} W/cm² peak intensity pulses for microsurgery applications focused in a 2.3 μ m spot thus offering improved spatial resolution. The lateral resolution of the system was also measured at difference distances away from the fiber facet and remains unchanged until about 300 μ m. More details about the change of the 3D point spread function and the field of view (FOV) of a MMF as a function of distance from the fiber facet in previous works on imaging through fiber probes [7,38,39,44–46]. With a range of 300 μ m within which the resolution remains unchanged, we believe that imaging of thick samples up to 200–300 μ m would be possible. The FOV of the system is mainly dependent on the fiber core diameter and the focusing distance from the fiber facet, which implies a FOV of more than 200 μ m for the larger core GRIN fiber. Furthermore, the size of the probe can remain 200–400 μ m since lens-less focusing and mechanic-less scanning is demonstrated by means of wavefront shaping. The main disadvantage of using a GRIN fiber endoscope is the post-calibration bending or misalignment of the system that would invalidate the measured TM of the fiber. To avoid that the use of a fiber cannula would keep the fiber from bending and it could be used as a thin needle. Even in this case, the final endoscope size would be in the order of about 1mm while offering FLA and TPF imaging capabilities with high spatial resolution.

5. TPF imaging feedback-based selective FLA

FLA is a technique with many biological and material processing applications. In most cases, the ablated area needs to be defined and a feedback mechanism is necessary. In this work, we demonstrate for the first time a MMF fiber probe that is able to perform FLA with high selectivity based on the TPF image of the sample, which is obtained through the same probe. TPF imaging provides high penetration depth for imaging of scattering samples such as biological tissues due to the use of infrared photons. In addition, the nonlinear character of the process results in higher resolution and sectioning than single-photon fluorescence imaging. Therefore, in our endoscope we use the TPF images as a guide for the FLA.

Biological tissues have significantly different properties than those of metals (for which we have demonstrated ablation through MCF's [20]). The basic content of biological samples is water and the FLA intensity threshold is close to that of water, on the order of $\sim 10^{12}$ W/cm² [10]. Because of the scattering properties of tissue, higher peak intensities than those for metals are needed to achieve subsurface laser ablation. Here we demonstrate that the 400 μ m core size GRIN probe with a peak intensity focus of 10^{13} W/cm² can provide enough power for tissue processing.

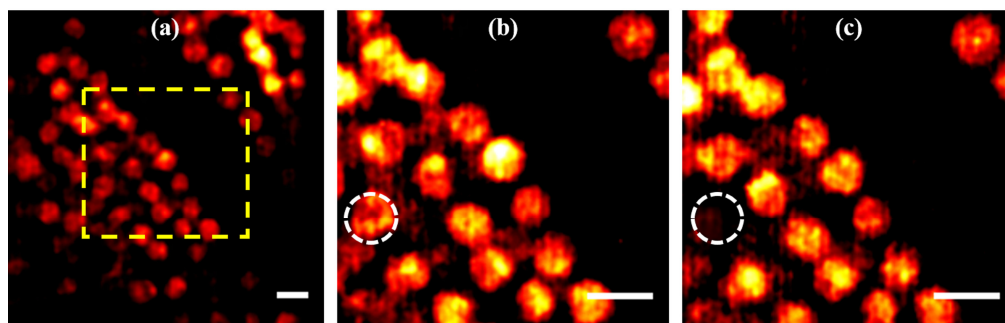


Fig. 3. TPF imaging of the Cochlear hair cell sample stained with PI in a) a wide image of the sample, b) zoomed region of interest (yellow square) and c) the same area as (b) after selectively ablating a cell marked in the white circle. The scale bar in all images is 10 μ m.

In the TPF imaging and FLA experiments presented in the following section, the maximum scanning window was 100 μ m x 100 μ m. In this range, there was some drop of the intensity at the sides of the window, which can be compensated by readjusting the phase masks on the SLM so that the intensity of the focus spots is equally distributed in the

scanning area. Our probe can provide TPF images (using $7.4 \times 10^{10} \text{ W/cm}^2$ intensity) of a wide field of view (FOV) of a fluorescently-stained Organ of Corti (prepared as detailed in Section 3), which contains precisely arranged rows of hair cells (Fig. 3(a)). We show that cellular level modifications can be obtained by digitally zooming in the area of interest (Fig. 3(b)) based on the TPF image in Fig. 3(a). By increasing the power above the ablation threshold for biological samples to $6.9 \times 10^{12} \text{ W/cm}^2$ [10], the beam destroys the selected cell. Afterwards, a second TPF image (Fig. 3(c)) confirms ablation of the targeted cell. Importantly, the laser ablation selectively induced damage only in the desired area, without affecting the TPF signal from the surrounding cells. This suggests that the ablation is likely limited to the cell area region approximately $7 \mu\text{m} \times 7 \mu\text{m}$. However, future work (beyond the scope of the current paper) is needed to assess and quantify possible collateral damage that the femtosecond laser may induce. In our experiments, the TPF image acquisition time and the scanning time for laser ablation is mainly limited by the SLM refresh rate which is at 20 Hz. As a result, to scan the area of a cell ($7 \mu\text{m} \times 7 \mu\text{m}$) it takes about 1 second.

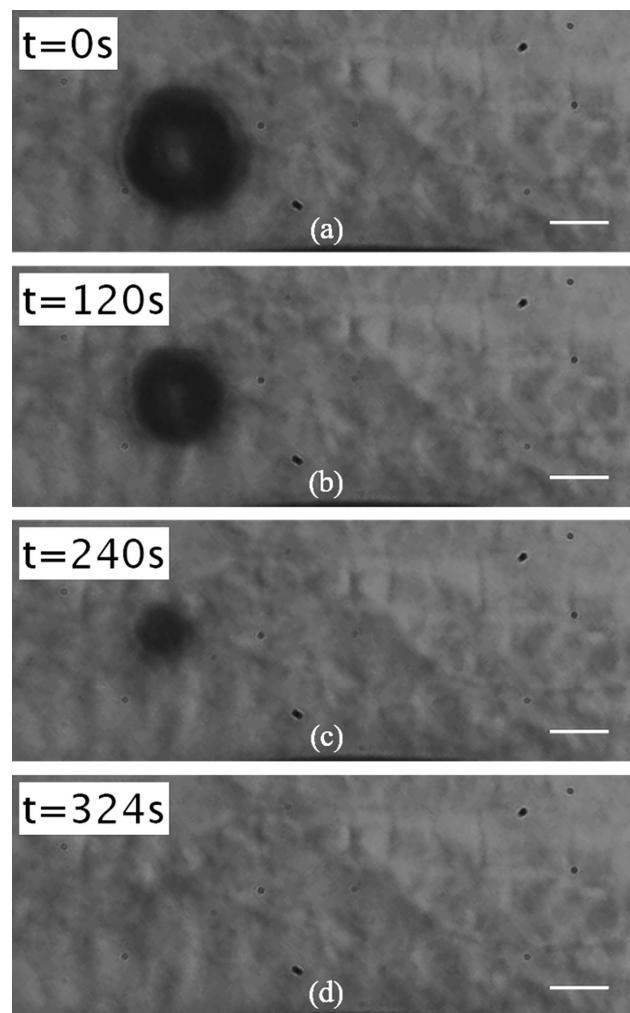


Fig. 4. BF images that show the time evolution of the bubble generated after FLA of a hair cell within the organ of Corti. $t = 0 \text{ s}$ is the time just after the FLA is finished. The scale bar in all the images is $10 \mu\text{m}$.

To confirm that FLA indeed results in specific cell loss as opposed to simple photobleaching of the specimen, we set a bright field imaging system in transmission at the distal side of the fiber (Fig. 1). We observe that at the FLA intensity levels, a bubble is formed in the sample shown (Fig. 4), consistent with ablation by the laser beam [10]. Since the sample is mounted in a supporting water-based medium, the bubble cannot easily escape and stays trapped until it collapses. As a consequence, in some cases, TPF imaging is not possible immediately after the ablation since the bubble prevents the light from the distal end of the fiber to be focused on the sample surface. We observed the time evolution, over 5 minutes, of the formation and disappearance of the bubble created after FLA using the BF imaging arm. There have been several studies related to the cavitation bubble dynamics after laser ablation of a material [10,47]. The mechanical properties and the laser parameters can affect the time evolution of the bubble [10]. We observed that even on the same sample the time needed until the bubble collapses varies from few seconds to few minutes. Further studies are needed to carefully evaluate the phenomena taking place in the sample when interacting with the laser beam.

6. Conclusions

We developed a GRIN fiber probe that combines the high sectioning and resolution of TPF imaging with the high-precision and low collateral damage properties of FLA. After careful investigation of the system performance, we identified the optimal parameters that allow TPF imaging of the Organ of Corti and selective FLA based on the images acquired through a single optical fiber. In addition, the 400 μm core size GRIN fiber shows great potential for FLA of an extended range of materials apart from biological samples because it provides a high peak intensity of $1.5 \times 10^{13} \text{ W/cm}^2$. Furthermore, the peak intensity provided is substantially above the ablation threshold for tissue, which may allow for subsurface laser ablation where the threshold is usually higher.

The integration of TPF imaging and FLA in the same fiber allows an optical guided feedback that may prove useful for medical investigation, diagnosis and therapy. For example, hearing loss, the majority of which originates from the inner ear, is genetically and microstructurally heterogeneous; thus, direct visualization of cochlear microanatomy would be useful to establish precise diagnosis and guide therapy, which could include morphological and functional modification of inner ear tissues. Furthermore, the cellular-level FLA selectivity presented in this work may find applications in Neurotology and neurosurgery, such as for the treatment of intracochlear or intralabyrinthine schwannomas. Genomic and proteomic analyses as well as laser microdissection of chromosomes are additional areas where selective laser ablation is of interest.

Funding

Swiss program: CEPF SFA, CERAMIC X.0: High-precision micro-manufacturing of ceramics; Bertarelli Program in Translational Neuroscience and Neuroengineering (10271).

Disclosures

The authors declare that there are no conflicts of interest related to this article.

References

1. A. Katzir, *Lasers and Optical Fibers in Medicine* (Elsevier, 2012).
2. F. Helmchen and W. Denk, "Deep tissue two-photon microscopy," *Nat. Methods* **2**(12), 932–940 (2005).
3. S. W. Perry, R. M. Burke, and E. B. Brown, "Two-photon and second harmonic microscopy in clinical and translational cancer research," *Ann. Biomed. Eng.* **40**(2), 277–291 (2012).
4. E. Capitaine, N. O. Moussa, C. Louot, S. M. Bardet, H. Kano, L. Duponchel, P. L  v  que, V. Couderc, and P. Leproux, "Fast epi-detected broadband multiplex CARS and SHG imaging of mouse skull cells," *Biomed. Opt. Express* **9**(1), 245–253 (2017).
5. P. J. Campagnola and L. M. Loew, "Second-harmonic imaging microscopy for visualizing biomolecular arrays in cells, tissues and organisms," *Nat. Biotechnol.* **21**(11), 1356–1360 (2003).

6. E. E. Morales-Delgado, S. Farahi, I. N. Papadopoulos, D. Psaltis, and C. Moser, "Delivery of focused short pulses through a multimode fiber," *Opt. Express* **23**(7), 9109–9120 (2015).
7. E. E. Morales-Delgado, D. Psaltis, and C. Moser, "Two-photon imaging through a multimode fiber," *Opt. Express* **23**(25), 32158–32170 (2015).
8. E. R. Andresen, G. Bouwmans, S. Monneret, and H. Rigneault, "Two-photon lensless endoscope," *Opt. Express* **21**(18), 20713–20721 (2013).
9. E. R. Andresen, S. Sivankutty, G. Bouwmans, O. Vainvinq, L. Gallais, S. Monneret, and H. Rigneault, "Towards two-photon lensless endoscopes: inter-core group delay compensation in a multi-core fiber," in E. Beaufepaire, P. T. C. So, F. Pavone, and E. M. Hillman, eds. (2015), p. 953605.
10. A. Vogel and V. Venugopalan, "Mechanisms of pulsed laser ablation of biological tissues," *Chem. Rev.* **103**(2), 577–644 (2003).
11. L. He, K. Sheehy, and W. Culbertson, "Femtosecond laser-assisted cataract surgery," *Curr. Opin. Ophthalmol.* **22**, 43 (2010).
12. J. Qiu, J. Neev, T. Wang, and T. E. Milner, "Deep subsurface cavities in skin utilizing mechanical optical clearing and femtosecond laser ablation," *Lasers Surg. Med.* **45**(6), 383–390 (2013).
13. J. Serbin, T. Bauer, C. Fallnich, A. Kasenbacher, and W. H. Arnold, "Femtosecond lasers as novel tool in dental surgery," *Appl. Surf. Sci.* **197–198**, 737–740 (2002).
14. G. Agrawal, *Nonlinear Fiber Optics* (Academic Press, 2001).
15. P. Russell, "Photonic crystal fibers," *Science* **299**(5605), 358–362 (2003).
16. Y. Wang, M. Alharbi, T. D. Bradley, C. Fourcade-Dutin, B. Debord, B. Beaudou, F. Gerôme, and F. Benabid, "Hollow-core photonic crystal fibre for high power laser beam delivery," *High Power Laser Science and Engineering* **1**(01), 17–28 (2013).
17. K. Subramanian, I. Gabay, O. Ferhanoglu, A. Shadfan, M. Pawlowski, Y. Wang, T. Tkaczyk, and A. Ben-Yakar, "Kagome fiber based ultrafast laser microsurgery probe delivering micro-Joule pulse energies," *Biomed. Opt. Express* **7**(11), 4639–4653 (2016).
18. B. Debord, M. Alharbi, L. Vincetti, A. Husakou, C. Fourcade-Dutin, C. Hoenninger, E. Mottay, F. Gerôme, and F. Benabid, "Multi-meter fiber-delivery and pulse self-compression of milli-Joule femtosecond laser and fiber-aided laser-micromachining," *Opt. Express* **22**(9), 10735–10746 (2014).
19. A. Shinde, S. M. Perinchery, and V. M. Murukeshan, "A targeted illumination optical fiber probe for high resolution fluorescence imaging and optical switching," *Sci. Rep.* **7**(1), 45654 (2017).
20. D. B. Conkey, N. Stasio, E. E. Morales-Delgado, M. Romito, C. Moser, and D. Psaltis, "Lensless two-photon imaging through a multicore fiber with coherence-gated digital phase conjugation," *J. Biomed. Opt.* **21**(4), 45002 (2016).
21. S. C. Warren, Y. Kim, J. M. Stone, C. Mitchell, J. C. Knight, M. A. A. Neil, C. Paterson, P. M. W. French, and C. Dunsby, "Adaptive multiphoton endomicroscopy through a dynamically deformed multicore optical fiber using proximal detection," *Opt. Express* **24**(19), 21474–21484 (2016).
22. F. Légaré, C. L. Evans, F. Ganikhanov, and X. S. Xie, "Towards CARS Endoscopy," *Opt. Express* **14**(10), 4427–4432 (2006).
23. I. N. Papadopoulos, S. Farahi, C. Moser, and D. Psaltis, "Focusing and scanning light through a multimode optical fiber using digital phase conjugation," *Opt. Express* **20**(10), 10583–10590 (2012).
24. D. Loterie, S. Farahi, I. Papadopoulos, A. Goy, D. Psaltis, and C. Moser, "Digital confocal microscopy through a multimode fiber," *Opt. Express* **23**(18), 23845–23858 (2015).
25. D. B. Conkey, E. Kakkava, T. Lanvin, D. Loterie, N. Stasio, E. Morales-Delgado, C. Moser, and D. Psaltis, "High power, ultrashort pulse control through a multi-core fiber for ablation," *Opt. Express* **25**(10), 11491–11502 (2017).
26. R. Di Leonardo and S. Bianchi, "Hologram transmission through multi-mode optical fibers," *Opt. Express* **19**(1), 247–254 (2011).
27. L. V. Amitonova, A. Descloux, J. Petschulat, M. H. Frosz, G. Ahmed, F. Babic, X. Jiang, A. P. Mosk, P. S. J. Russell, and P. W. H. Pinkse, "High-resolution wavefront shaping with a photonic crystal fiber for multimode fiber imaging," *Opt. Lett.* **41**(3), 497–500 (2016).
28. R. Kuschmierz, E. Scharf, N. Koukourakis, and J. W. Czarke, "Self-calibration of lensless holographic endoscope using programmable guide stars," *Opt. Lett.* **43**(12), 2997–3000 (2018).
29. E. R. Andresen, S. Sivankutty, G. Bouwmans, L. Gallais, S. Monneret, and H. Rigneault, "Measurement and compensation of residual group delay in a multi-core fiber for lensless endoscopy," *J. Opt. Soc. Am. B* **32**(6), 1221 (2015).
30. Y. Li, J. Jing, J. Yu, B. Zhang, T. Huo, Q. Yang, and Z. Chen, "Multimodality endoscopic optical coherence tomography and fluorescence imaging technology for visualization of layered architecture and subsurface microvasculature," *Opt. Lett.* **43**(9), 2074–2077 (2018).
31. J. Xi, Y. Chen, Y. Zhang, K. Murari, M.-J. Li, and X. Li, "Integrated multimodal endomicroscopy platform for simultaneous en face optical coherence and two-photon fluorescence imaging," *Opt. Lett.* **37**(3), 362–364 (2012).
32. I. M. Vellekoop and A. P. Mosk, "Focusing coherent light through opaque strongly scattering media," *Opt. Lett.* **32**(16), 2309–2311 (2007).
33. M. Plöschner, T. Tyc, and T. Čížmár, "Seeing through chaos in multimode fibres," *Nat. Photonics* **9**(8), 529–535 (2015).

34. X. Chen, K. L. Reichenbach, and C. Xu, "Experimental and theoretical analysis of core-to-core coupling on fiber bundle imaging," *Opt. Express* **16**(26), 21598–21607 (2008).
35. Arnaud Brignon, *Coherent Laser Beam Combining* (Wiley-VCH Verlag GmbH & Co. KGaA, 2013).
36. K. L. Reichenbach and C. Xu, "Numerical analysis of light propagation in image fibers or coherent fiber bundles," *Opt. Express* **15**(5), 2151–2165 (2007).
37. K. Okamoto, *Fundamentals of Optical Waveguides, Second Edition*, 2 edition (Academic Press, 2005).
38. I. N. Papadopoulos, S. Farahi, C. Moser, and D. Psaltis, "High-resolution, lensless endoscope based on digital scanning through a multimode optical fiber," *Biomed. Opt. Express* **4**(2), 260–270 (2013).
39. S. Sivankutty, E. R. Andresen, R. Cossart, G. Bouwmans, S. Monneret, and H. Rigneault, "Ultra-thin rigid endoscope: two-photon imaging through a graded-index multi-mode fiber," *Opt. Express* **24**(2), 825–841 (2016).
40. D. J. McCabe, A. Tajalli, D. R. Austin, P. Bondareff, I. A. Walmsley, S. Gigan, and B. Chatel, "Spatio-temporal focusing of an ultrafast pulse through a multiply scattering medium," *Nat. Commun.* **2**(1), 447 (2011).
41. S. Popoff, G. Lerosey, M. Fink, A. C. Boccara, and S. Gigan, "Controlling Light Through Optical Disordered Media : Transmission Matrix Approach," 1107.5285 (2011).
42. O. Tzang, A. M. Caravaca-Aguirre, K. Wagner, and R. Piestun, "Adaptive wavefront shaping for controlling nonlinear multimode interactions in optical fibres," *Nat. Photonics* **12**(6), 368–374 (2018).
43. D. Psaltis, E. Kakkava, N. Stasio, D. B. Conkey, and C. Moser, "Femtosecond pulse delivery through multi-core fibers for imaging and ablation," in Z. Liu, ed. (SPIE, 2017), p. 30.
44. M. Plöschner, V. Kollárová, Z. Dostál, J. Nylk, T. Barton-Owen, D. E. K. Ferrier, R. Chmelík, K. Dholakia, and T. Čižmár, "Multimode fibre: Light-sheet microscopy at the tip of a needle," *Sci. Rep.* **5**(1), 18050 (2015).
45. A. Descloux, L. V. Amitonova, and P. W. H. Pinkse, "Aberrations of the point spread function of a multimode fiber due to partial mode excitation," *Opt. Express* **24**(16), 18501–18512 (2016).
46. S. Rosen, D. Gilboa, O. Katz, and Y. Silberberg, "Focusing and Scanning through Flexible Multimode Fibers without Access to the Distal End," 8 (n.d.).
47. K. Nakamura, Y. Sora, H. Y. Yoshikawa, Y. Hosokawa, R. Murai, H. Adachi, Y. Mori, T. Sasaki, and H. Masuhara, "Femtosecond laser-induced crystallization of protein in gel medium," *Appl. Surf. Sci.* **253**(15), 6425–6429 (2007).